

Versatility and robustness of Gaussian random fields for modelling random media

John A Quintanilla^{1,5}, Jordan T Chen^{2,6}, Richard F Reidy³ and Andrew J Allen⁴

¹ Department of Mathematics, PO Box 311430, University of North Texas, Denton, TX 76203, USA

² Texas Academy of Mathematics and Science, PO Box 305309, University of North Texas, Denton, TX 76203, USA

³ Department of Materials Science, PO Box 305310, University of North Texas, Denton, TX 76203, USA

⁴ Ceramics Division, National Institute of Standards and Technology, 100 Bureau Drive, Stop 8523, Gaithersburg, MD 20899, USA

E-mail: jquintanilla@unt.edu, theevenprime2@yahoo.com, reidy@unt.edu and andrew.allen@nist.gov

Received 29 September 2006, in final form 19 February 2007

Published 1 May 2007

Online at stacks.iop.org/MSMSE/15/S337

Abstract

One of the authors (JAQ) has recently introduced a method of modelling random materials using excursion sets of Gaussian random fields. This method uses convex quadratic programming to find the optimal admissible field autocorrelation function, providing both theoretical and computational advantages over other techniques such as simulated annealing. In this paper, we discuss the application of this algorithm to model various aerogel systems given small-angle neutron scattering data. We also present new results concerning the robustness of this method.

(Some figures in this article are in colour only in the electronic version)

1. Introduction

Models based on Gaussian random fields (GRFs) have been employed in the literature to study a variety of material systems [1–19]. These GRF models are often constructed using the two-point phase probability function $S_2(r)$, defined to be the probability that two points \mathbf{x} and \mathbf{y} with $r = |\mathbf{x} - \mathbf{y}|$ both lie in the solid phase. Throughout this paper, we will assume that S_2 depends only on the distance r between the two points \mathbf{x} and \mathbf{y} .

We define the phase autocorrelation function as

$$\chi(r) = S_2(r) - \phi^2,$$

⁵ Author to whom any correspondence should be addressed.

⁶ Permanent address: 1825 Skyline Drive, Sherman, Texas 75092, USA.

where ϕ is the volume fraction of the solid phase. Many techniques for measuring $\chi(r)$ for random materials have been proposed in the literature, including the use of small-angle scattering data as described in section 2.

In this paper, we consider isotropic GRFs Y with mean 0 and variance 1. Such GRFs are completely characterized by the field autocorrelation function $G(r) = \langle Y(\mathbf{x})Y(\mathbf{y}) \rangle$, where $r = |\mathbf{x} - \mathbf{y}|$. (This function should not be confused with the phase autocorrelation function $\chi(r)$.) It can be shown that $G(r)$ can serve as a field autocorrelation function if and only if $G(0) = 1$ and $G(r)$ is a positive-definite function, so that the Fourier transform

$$\tilde{G}(k) = \sqrt{\frac{2}{\pi}} \int_0^\infty r^2 G(r) \frac{\sin kr}{kr} dr \quad (1)$$

is nonnegative. We notice that the inverse Fourier transform is defined by

$$G(r) = \sqrt{\frac{2}{\pi}} \int_0^\infty k^2 \tilde{G}(k) \frac{\sin kr}{kr} dk, \quad (2)$$

so that the condition $G(0) = 1$ becomes

$$1 = \sqrt{\frac{2}{\pi}} \int_0^\infty k^2 \tilde{G}(k) dk. \quad (3)$$

As we will see, this condition will be used in the algorithm described in section 2.

A one-cut GRF model (also called an excursion set) for a specified threshold α is defined as follows: assign all points \mathbf{x} so that $Y(\mathbf{x}) \geq \alpha$ to phase 1, while all other points are assigned to phase 2. The value of α may be computed from the volume fraction ϕ through the relationship (13), as discussed below.

Loosely speaking, the primary goal of modelling is to choose $G(r)$ so that the resulting one-cut GRF model fits the experimental data. One method of achieving this is by assuming that $G(r)$ has some given parametrized form, such as

$$G(r) = \frac{e^{-r/a} - (c/a)e^{-r/c}}{1 - (c/a)} \frac{\sin(br)}{br}. \quad (4)$$

This particular function is known to be positive definite if $a > c > 0$ and $b > 0$, and so the problem of finding the best $G(r)$ reduces to optimizing over a portion of \mathbb{R}_+^3 [6]. However, there is no reason *a priori* to think that the optimal $G(r)$ belongs to this or any other predetermined parametrized family of positive-definite functions.

One of the authors recently introduced a new algorithm which searches over discretizations of all positive-definite functions to find the optimal field autocorrelation function [20]. This discretization reduces the optimization problem to a convex quadratic program with linear constraints, thus optimizing over all positive-definite functions instead of only those within some parametrized family. Experience has shown that this algorithm is very efficient computationally, typically using only seconds of runtime on a desktop microcomputer.

In section 2, we describe the convex quadratic programming algorithm for three-dimensional models using scattering data as input. In section 3, we present results of this algorithm for various aerogels. As seen in figures 1–4, the theoretical scattering curves of the GRF models provide an excellent fit to the experimental scattering data, thus indicating the viability of the GRF model for assessing the microstructure of these aerogels. Visualizations of these aerogels are presented in figures 5–13. We also discuss the robustness of this algorithm by considering perturbations when the source data is perturbed by small errors consistent with uncertainties which arise from experimental measurement.

2. Presentation of algorithm

In this section, we present the algorithm for computing the optimal one-cut GRF model given the scattering data. We will assume that, at M different frequencies $q_1 < \dots < q_M$ (also called scattering vectors in the parlance of experimental work), the scattering intensity data I_1, \dots, I_M has been measured. We also assume that the volume fraction ϕ is known. The output of this algorithm will be the field-field correlation function $G(r)$ which defines the optimal one-cut GRF model. More discussion about this algorithm may be found in [20].

Step 1. Compute $\chi(r)$ from the scattering data $I(q)$.

In the absence of multiple scattering, the functions $\chi(r)$ and $I(q)$ are related by [21]

$$\chi(r) = \frac{1}{2\pi^2 V \eta^2} \int_0^\infty [I(q) - I^*] q^2 \frac{\sin qr}{qr} dq. \tag{5}$$

In this formula, I^* is the background noise, V is the volume of the material and η is the scattering density of the solid phase.

In practice, formula (5) cannot be used alone because $\chi(r)$ must be a positive-definite function [22], a requirement that may be violated due to both experimental and numerical uncertainties. Instead, we will use the present algorithm to construct a GRF model whose phase autocorrelation function $X(r)$ is as close as possible to the $\chi(r)$ derived from (5).

Since the integral in (5) is over a semi-infinite interval, we will need to estimate the asymptotic behaviour of the intensity data. We do this using the expansion [22]

$$I(q) - I^* \sim \frac{a}{q^4} + \frac{b}{q^6} + \frac{c}{q^8} \quad \text{as } q \rightarrow \infty. \tag{6}$$

The background noise I^* is estimated to be the number that gives the best approximation to this asymptotic behaviour. Furthermore, the values of a , b and c are obtained by least-squares fitting to some subset of the largest frequencies q_j used in the experiment.

Using this approximation, we will replace (5) by

$$\chi(r) \approx \frac{A_1(r) + A_2(r)}{2\pi^2 V \eta^2}, \tag{7}$$

where

$$A_1(r) = \int_0^Q [I(q) - I^*] q^2 \frac{\sin qr}{qr} dq,$$

$$A_2(r) = \int_Q^\infty \left(\frac{a}{q^2} + \frac{b}{q^4} + \frac{c}{q^6} \right) \frac{\sin qr}{qr} dq$$

and $Q = q_M = \max\{q_j\}$. For a given value of r , $A_1(r)$ may be approximated numerically:

$$A_1(r) \approx \sum_{j=1}^{M-1} \left(\frac{q_{j+1} - q_j}{2} \right) \left(I_j^* q_j^2 \frac{\sin q_j r}{q_j r} + I_{j+1}^* q_{j+1}^2 \frac{\sin q_{j+1} r}{q_{j+1} r} \right), \tag{8}$$

where $I_j^* = I_j - I^*$ is the background-corrected intensity at q_j . Also, $A_2(r)$ may be computed analytically:

$$A_2(r) = \frac{360aQ^4 + 30bQ^2(2 - Q^2r^2) + c(24 - 2Q^2r^2 + Q^4r^4)}{720Q^5} \cos(Qr)$$

$$+ \frac{360aQ^4 + 30bQ^2(6 - Q^2r^2) + c(120 - 6Q^2r^2 + Q^4r^4)}{720Q^6r} \sin(Qr)$$

$$+ \frac{Q^6r^2(2 - \pi)(360a - 30br^2 + cr^4)}{1440Q^6r} \text{Si}(Qr), \tag{9}$$

where $\text{Si}(x)$ is the sine integral function

$$\text{Si}(x) = \int_0^x \frac{\sin t}{t} dt.$$

To use (7), we will also need to compute the constant $V\eta^2$. To do this, we will use the fact that $\chi(0) = \phi - \phi^2$. Taking the limit $r \rightarrow 0$ in (7) and rearranging, we see that [21]

$$V\eta^2 = \frac{A_1(0) + A_2(0)}{2\pi^2(\phi - \phi^2)},$$

where

$$A_1(0) = \int_0^Q q^2 [I(q) - I^*] dq \approx \sum_{j=1}^{M-1} \left(\frac{q_{j+1} - q_j}{2} \right) (I_j^* q_j^2 + I_{j+1}^* q_{j+1}^2) \quad (10)$$

and

$$A_2(0) = \int_Q^\infty \left(\frac{a}{q^2} + \frac{b}{q^4} + \frac{c}{q^6} \right) dq = \frac{a}{Q} + \frac{b}{3Q^3} + \frac{c}{5Q^5}. \quad (11)$$

Summarizing, the phase autocorrelation function $\chi(r)$ is computed from the volume fraction ϕ and the scattering data $\{I_j\}$ at frequencies $\{q_j\}$ by the formula

$$\chi(r) \approx (\phi - \phi^2) \frac{A_1(r) + A_2(r)}{A_1(0) + A_2(0)}, \quad (12)$$

where (8)–(11) define the individual terms in (12) and the parameters I^* , a , b and c are determined by a certain least-squares fit of the scattering data to (6).

Step 2. Compute the cut parameter α . To do this, we will use the known formula for the volume fraction of the GRF model:

$$\phi = \frac{1}{\sqrt{2\pi}} \int_{-\infty}^{\alpha} e^{-t^2/2} dt. \quad (13)$$

Since ϕ is assumed to be known, (13) can be used to solve for α by using a numerical technique like the Newton–Raphson method. Alternatively, solving for α in (13) is equivalent to finding a percentile of a standard normal distribution, and many mathematical software packages as well as hand-held scientific calculators have built-in functions for this purpose.

Step 3. Compute the field autocorrelation function $g(r)$. This may be done by using the known expression [23]

$$\chi(r) = \frac{1}{2\pi} \int_0^{g(r)} \frac{1}{\sqrt{1-t^2}} \exp\left(-\frac{\alpha^2}{1+t}\right) dt, \quad (14)$$

where α and $\chi(r)$ were computed in the previous two steps. This may be accomplished by using the Newton–Raphson method: fix r and define

$$F(z) = -\chi(r) + \frac{1}{2\pi} \int_0^z \frac{1}{\sqrt{1-t^2}} \exp\left(-\frac{\alpha^2}{1+t}\right) dt. \quad (15)$$

Then the iterative sequence defined by

$$z_{n+1} = z_n - \frac{F(z_n)}{F'(z_n)} = z_n + \frac{\chi(r) - \frac{1}{2\pi} \int_0^{z_n} \frac{1}{\sqrt{1-t^2}} \exp\left(-\frac{\alpha^2}{1+t}\right) dt}{\frac{1}{2\pi\sqrt{1-z_n^2}} \exp\left(-\frac{\alpha^2}{1+z_n}\right)}$$

will converge to the value z^* so that $F(z^*) = 0$; the above integral should be computed numerically. The function $g(r)$ is defined to be this value z^* . This process is then repeated to obtain values of $g(r)$ for all r on some discretization.

Step 4. Compute the Fourier transform $\tilde{g}_i = \tilde{g}(i\Delta k)$ for $i = 1, \dots, N$, where N and Δk are chosen to specify a discretization of the Fourier transform of $\tilde{g}(k)$. This may be done by numerically computing

$$\tilde{g}(k) = \sqrt{\frac{2}{\pi}} \int_0^\infty r^2 g(r) \frac{\sin kr}{kr} dr. \quad (16)$$

The values of $g(r)$ computed in the previous step are used to evaluate (16). This computation may be done by using any standard numerical integration technique; alternatively, a fast Fourier transform may be employed [24].

To arise from a GRF model, the function $\tilde{g}(k)$ should be nonnegative. However, as discussed above, we will not expect each of the N numbers computed at this step to be nonnegative.

Step 5. Compute a nonnegative approximation \tilde{G}_i for $i = 1, \dots, N$ by solving the following convex quadratic programming problem:

$$\begin{aligned} \text{Minimize} \quad & \sum_{i=1}^N i^2 [\tilde{g}_i - \tilde{G}_i]^2 \\ \text{subject to} \quad & \tilde{G}_i \geq 0 \quad \text{for } i = 1, \dots, N, \\ & N^2 \tilde{G}_N + \sum_{i=1}^{N-1} 2i^2 \tilde{G}_i = \frac{\sqrt{2\pi}}{(\Delta k)^3}. \end{aligned} \quad (17)$$

This is the key step of the present algorithm, permitting a broad search over all positive-definite functions instead of only those within a predetermined parametrized family.

The convex quadratic programming problem (17) discretizes the problem of finding the closest (under the $L^2(\mathbb{R}^3)$ norm) nonnegative function $\tilde{G}(k)$ to $\tilde{g}(k)$ given the constraint (3), since the discrete representations of these two functions are the sequences $\{\tilde{G}_i\}$ and $\{\tilde{g}_i\}$, respectively. (The i^2 term in the objective function is necessary to minimize the $L^2(\mathbb{R}^3)$ norm.) In light of Parseval's equality, this minimization problem is equivalent to finding the closest positive-definite function $G(r)$ to $g(r)$ given the constraint $G(0) = 1$.

We now discuss the constraints of the optimization problem (17). The first constraint requires that each \tilde{G}_i be nonnegative, so that $G(r)$ is a positive-definite function. The second constraint arises from discretizing the requirement (3) with the trapezoid rule. These are the two constraints for a field autocorrelation function in a GRF model, as discussed in the introduction.

To solve (17), we used the '-m' option of the software package LOQO [25], which supports an extension of the standard MPS format [26,27] to solve optimization problems with quadratic objective functions and linear constraints.⁷ We wrote our own C++ program which created the necessary MPS files implementing (17) using the \tilde{g}_i as input; LOQO was subsequently executed using these MPS files. LOQO was created by Robert Vanderbei and is licensed by Princeton University; information about this software may be found at www.princeton.edu/~rvdb.

⁷ Certain commercial equipment, instruments or materials are identified in this document. Such identification does not imply recommendation or endorsement by the National Institute of Standards and Technology, nor does it imply that the products identified are necessarily the best available for the purpose.

Step 6. Evaluate $G(r)$, the optimal positive-definite approximation to $g(r)$. This may be done by numerically computing the inverse Fourier transform (2), which we repeat here:

$$G(r) = \sqrt{\frac{2}{\pi}} \int_0^\infty k^2 \tilde{G}(k) \frac{\sin kr}{kr} dk.$$

In this expression, the function \tilde{G} is discretized by $\tilde{G}(i\Delta k) = \tilde{G}_i$, which were computed in the previous step. The computation of $G(r)$ may be accomplished with either numerical integration or a fast Fourier transform.

The field autocorrelation function $G(r)$ and the cut level α specify the optimal one-cut GRF model, permitting visualizations of the model. We note that some visualization algorithms directly use $\tilde{G}(k)$ instead of $G(r)$; for these algorithms, visualizations may be produced without step 6.

To check how well this optimal model fits the original scattering data, we perform two additional steps.

Step 7. Evaluate $X(r)$, the optimal phase autocorrelation function for $\chi(r)$ arising from a one-cut GRF model. This may be done by numerically computing the integral

$$X(r) = \frac{1}{2\pi} \int_0^{G(r)} \frac{1}{\sqrt{1-t^2}} \exp\left(-\frac{\alpha^2}{1+t}\right) dt, \quad (18)$$

which is essentially the same integral as (14). This calculation is done over some discretized values of r .

Step 8. Compute the theoretical intensity data. This may be done by using the above discretized values of $X(r)$ and a numerical evaluation of the integral

$$I(q) = I^* + V\eta^2 \int_0^\infty 4\pi r^2 X(r) \frac{\sin qr}{qr} dr, \quad (19)$$

which is essentially the inverse transform of (5). This may be done by either numerical integration or a fast Fourier transform. The one-cut GRF model may be validated by comparing the graph of $I(q)$ with the original scattering data.

3. Results

3.1. Comparison with experimental Data

In figures 1–3, we show small-angle neutron scattering (SANS) data for seven different tetramethoxysilane (TMOS) aerogels. The TMOS aerogels were synthesized from tetramethoxysilane (TMOS, $\text{Si}(\text{OCH}_3)_4$) in ethanol and aqueous solutions of varying pH. The samples were gelled and aged for three days in ethanol in 1 cm vials at 25 °C. The calculated solid-phase volume fractions of these seven TMOS aerogels ranged from 2.4% to 10.1%.

In figure 4, we show SANS data for two different triethoxysilane (TES) aerogels. Triethoxysilane ($\text{H-Si}(\text{OC}_2\text{H}_5)_3$) was dissolved in ethanol and reacted with 18.2 MΩ water to form TES aerogels. The calculated solid-phase volume fractions of these two TES aerogels were 8.0% and 7.3%, respectively.

The small-angle neutron scattering experiments were conducted on the NIST/NSF NG3 and NG7 30m SANS instruments at the NIST Center for Neutron Research (NCNR). Previous work on aerogels similar to TMOS have shown that these types of materials are made up of near periodic arrangements of globular moieties [28].

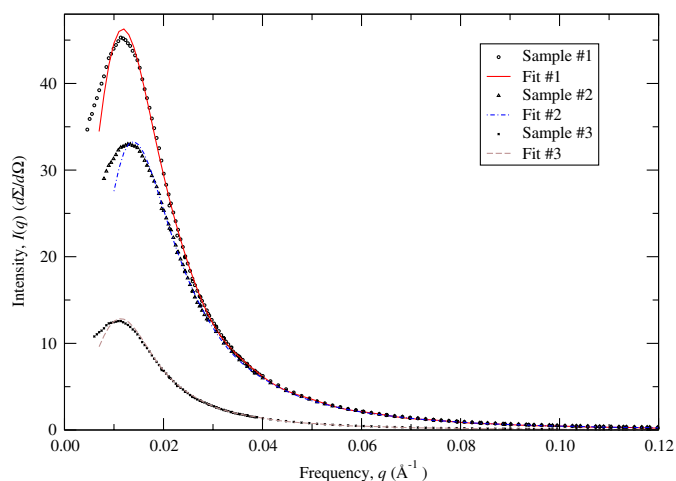


Figure 1. Small-angle neutron scattering data for three different TMOS aerogels and the theoretical scattering functions for the corresponding GRF models. In this and the following figures, standard deviation uncertainties in the experimental data are not significantly greater than the size of the symbols and are indicated by slight scatter in the data points. We see that convex quadratic programming produces models which provide an excellent fit to the experimental data. Visualizations for these aerogels are shown in figures 5–7.

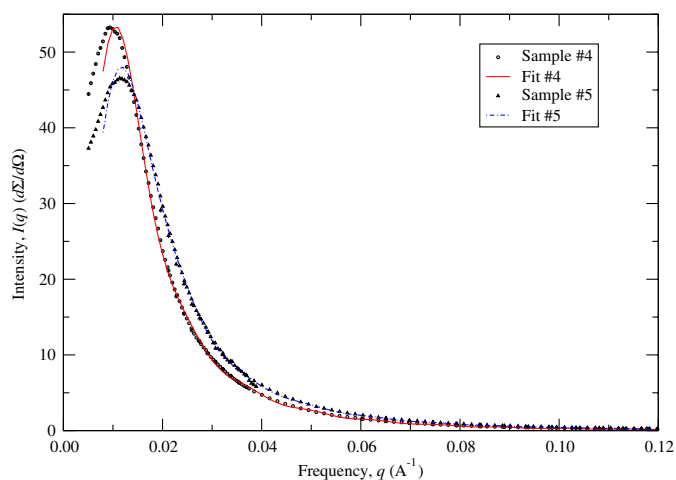


Figure 2. As in figure 1, but for two other TMOS aerogels. Visualizations for these aerogels are shown in figures 8 and 9.

For these aerogels, figures 1–4 show the intensity data points $I(q)$ (also known to experimentalists as the absolute calibrated differential scattering cross-section $d\Sigma/d\Omega$) as a function of the scattering vector q (in \AA^{-1}). Standard deviation uncertainties in the experimental data are not significantly greater than the size of the symbols and are indicated by a slight scatter in the data points.

Also shown in these figures are the theoretical scattering curves for the optimal GRF models. As discussed above, the SANS data and the volume fractions are used as input to construct these optimal GRF models. We see that the optimal GRF models provide excellent

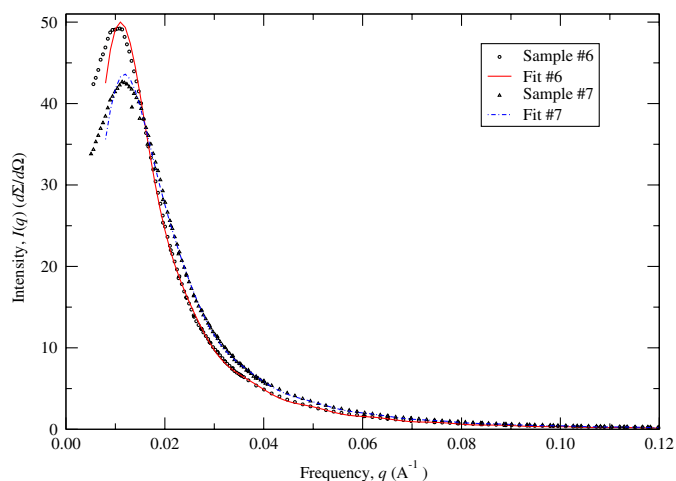


Figure 3. As in figures 1 and 2, but for two other TMOS aerogels. Visualizations for these aerogels are shown in figures 10 and 11.

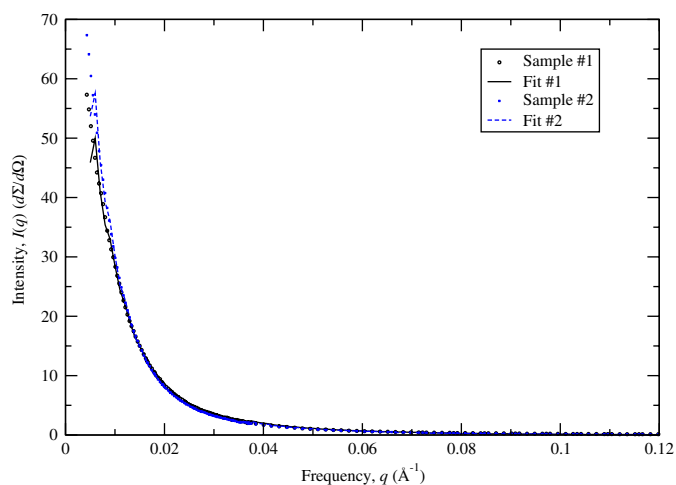


Figure 4. As in figures 1–3, except for two different TES aerogels. Once again, the GRF models have theoretical intensity curve which provide an excellent fit to the experimental data. These fits show the versatility of the GRF model, since the source scattering data has a qualitatively different shape in this figure than in figures 1–3. Visualizations for these aerogels are shown in figures 12 and 13.

fits to the experimental data, suggesting that these GRF models are reasonable for these aerogels.

The GRF model may be used to produce visualizations of aerogels. In figures 5–11, we show visualizations of the seven TMOS aerogels modelled in figures 1–3. In figures 12 and 13, we show visualizations of the TES aerogels modelled in figure 4. These visualizations were generated using the turning-bands method [29,30] for generating Gaussian random fields. Since these visualizations are randomly generated, they should be considered as statistical and not a deterministic rendering of the microstructure.

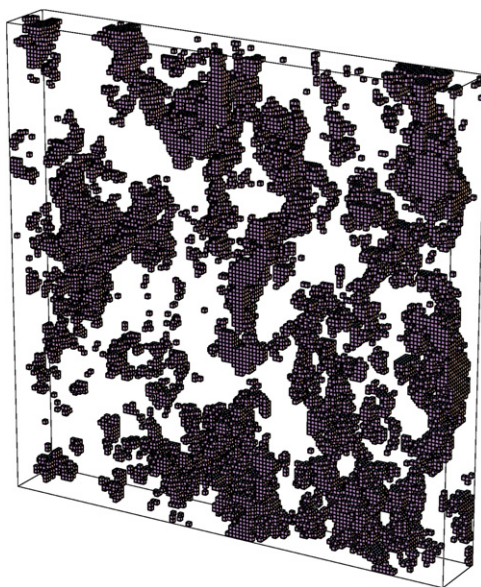


Figure 5. A visualization of the first TMOS aerogel (solid volume fraction of 10.1%). The scattering curve for this aerogel is in figure 1. The dimensions of this visualization are $1500 \times 1500 \times 187.5 \text{ \AA}$.

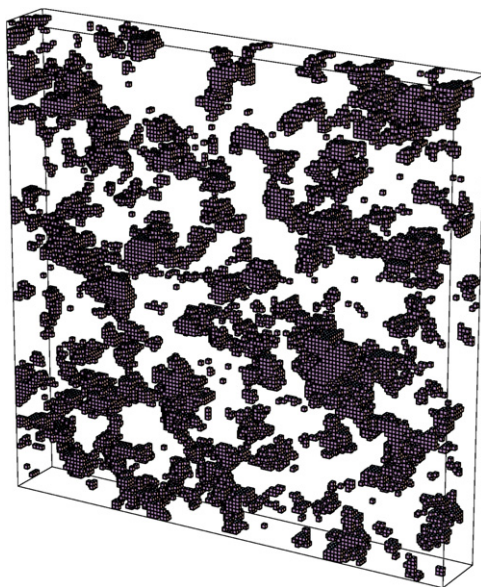


Figure 6. A visualization of the second TMOS aerogel (solid volume fraction of 9.7%). The scattering curve for this aerogel is in figure 1. The dimensions of this visualization are $1500 \times 1500 \times 187.5 \text{ \AA}$.

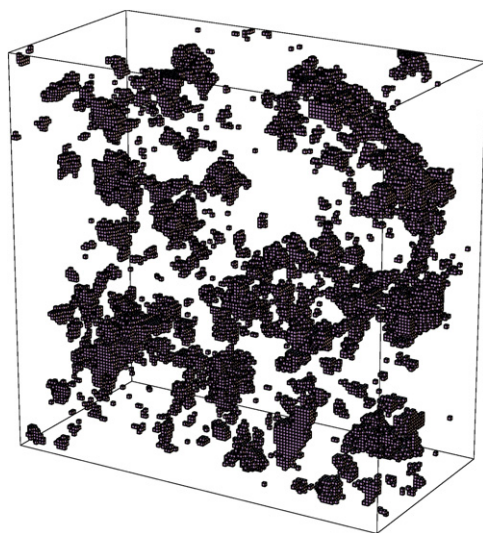


Figure 7. A visualization of the third TMOS aerogel (solid volume fraction of 2.4%). The scattering curve for this aerogel is in figure 1. The dimensions of this visualization are $1500 \times 1500 \times 375 \text{ \AA}$; we show a thicker visualization given the lower volume fraction of this aerogel.

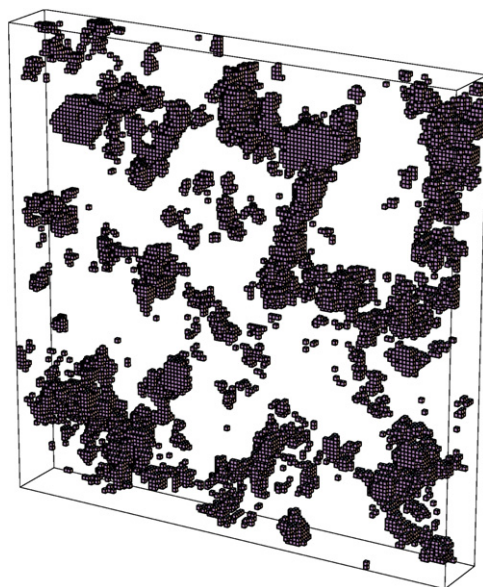


Figure 8. A visualization of a fourth TMOS aerogel (solid volume fraction of 5.6%). The scattering curve for this aerogel is in figure 2. The dimensions of this visualization are $1500 \times 1500 \times 187.5 \text{ \AA}$.

3.2. Low wavenumbers

The fits in figures 1–4 are quite close for most values of q . However, the fits tend to diverge from the data for low values of q . To identify the source of this divergence, we analysed the different scattering curves that arise if the discretization parameters N and Δk (defined in step 4) are modified. From this analysis, we are confident that this discrepancy is due to

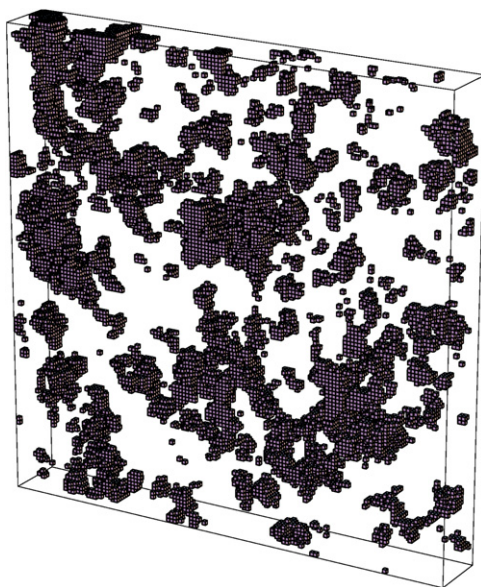


Figure 9. A visualization of a fifth TMOS aerogel (solid volume fraction of 9.3%). The scattering curve for this aerogel is in figure 2. The dimensions of this visualization are $1500 \times 1500 \times 187.5 \text{ \AA}$.

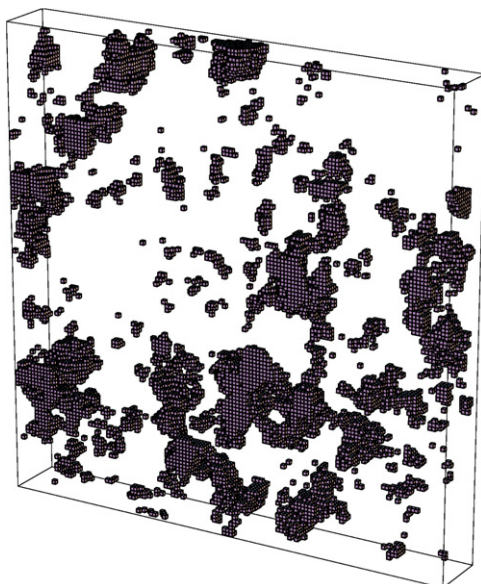


Figure 10. A visualization of a sixth TMOS aerogel (solid volume fraction of 5.3%). The scattering curve for this aerogel is in figure 3. The dimensions of this visualization are $1500 \times 1500 \times 187.5 \text{ \AA}$.

computational error inherent in the discretizations used in the above algorithm, especially the Fourier transforms computed in steps 4, 6 and 8. We do not think that these discrepancies represent a fundamental inability of the GRF model to replicate the experimental scattering curves.

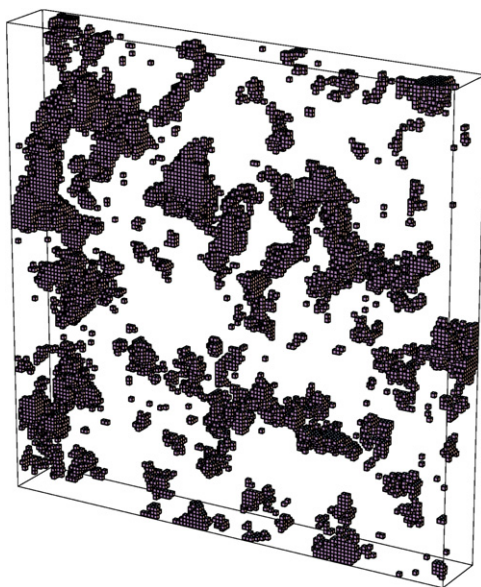


Figure 11. A visualization of a seventh TMOS aerogel (solid volume fraction of 8.7%). The scattering curve for this aerogel is in figure 3. The dimensions of this visualization are $1500 \times 1500 \times 187.5 \text{ \AA}$.

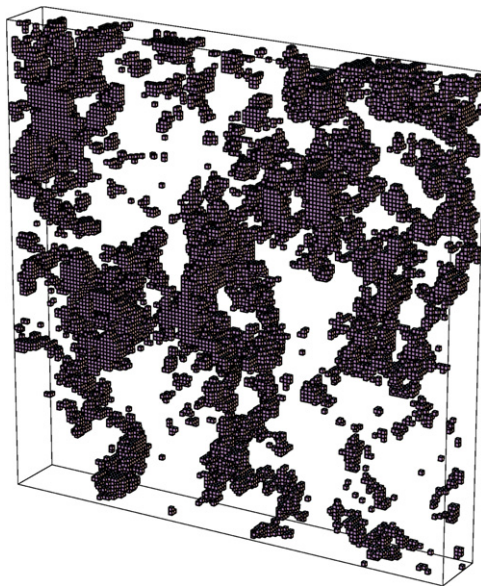


Figure 12. A visualization of the first TES aerogel (solid volume fraction of 8.0%). The scattering curve for this aerogel is in figure 4. The dimensions of this visualization are $1500 \times 1500 \times 187.5 \text{ \AA}$.

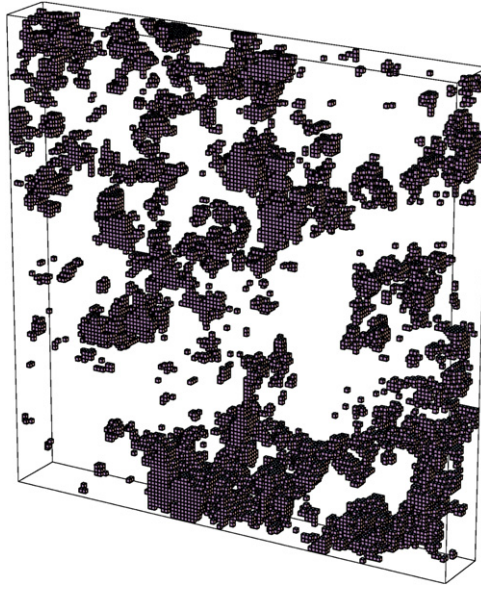


Figure 13. A visualization of the second TES aerogel (solid volume fraction of 7.3%). The scattering curve for this aerogel is in figure 4. The dimensions of this visualization are $1500 \times 1500 \times 187.5 \text{ \AA}$.

We note that the experimental uncertainties for small q are larger because of poor statistics in this region and/or local ordering of the structure. We also note that, in principle, it is possible to approximate the theoretical intensity curve $I(q)$ for low values of q by eliminating one of the Fourier transforms. For example, we may formally compute $I(q)$ at $q = 0$ from (18) and (19), as follows:

$$\begin{aligned} I(0) &= I^* + V\eta^2 \int_0^\infty 4\pi r^2 X(r) dr \\ &= I^* + 2\pi V\eta^2 \int_0^\infty \int_0^{G(r)} \frac{r^2}{\sqrt{1-t^2}} \exp\left(-\frac{\alpha^2}{1+t}\right) dt dr. \end{aligned}$$

If the function G turns out to be monotonic, then we may reverse the order of integration, obtaining

$$\begin{aligned} I(0) &= I^* + 2\pi V\eta^2 \int_0^1 \int_0^{G^{-1}(t)} \frac{r^2}{\sqrt{1-t^2}} \exp\left(-\frac{\alpha^2}{1+t}\right) dr dt \\ &= I^* + \frac{2\pi V\eta^2}{3} \int_0^1 \frac{[G^{-1}(t)]^3}{\sqrt{1-t^2}} \exp\left(-\frac{\alpha^2}{1+t}\right) dt. \end{aligned}$$

This last integral may then be computed numerically.

However, in practice, we observed that the output $G(r)$ was not monotonic. Therefore, to use this idea for computing $I(0)$, we would need to reverse the order of integration as

$$I(0) = I^* + \frac{2\pi V\eta^2}{3} \int_0^1 \sum_i \frac{[b_i(t)]^3 - [a_i(t)]^3}{\sqrt{1-t^2}} \exp\left(-\frac{\alpha^2}{1+t}\right) dt,$$

where $a_i(t)$ and $b_i(t)$ are defined by

$$\bigcup_i [a_i(t), b_i(t)] = \{r \mid G(r) \leq t\}. \quad (20)$$

Careful measurement of the endpoints $a_i(t)$ and $b_i(t)$ would then be critical for the computation of $I(0)$. However, doing so would require a very precise evaluation of $G(r)$ in step 6 of the algorithm of section 2. A similar analysis may be conducted for small but positive wavenumbers q .

With the computational resources available at the time of writing this, however, it appears that such an analysis is beyond the numerical accuracy of the algorithm.

3.3. Robustness

In the previous calculations, we assumed that both the volume fraction ϕ and the scattering data $I(q_j)$ were exactly known. However, in practice, the measurement of both quantities are subject to experimental uncertainties. In this section, we study the robustness of the algorithm in section 2 with respect to these measurement errors.

To do this, we reinvestigated the tetraethoxysilane (TEOS) aerogel which was modelled in [20] and created 100 intensity curves which were consistent with experimental errors. Specifically, we perturbed the scattering data $I(q_j)$ by Gaussian random deviates whose standard deviations matched the standard deviations observed from the experiment. For the TEOS intensity data, the relative experimental error in the measurement of $I(q_j)$ averaged 0.54%, with a maximum relative error of 2.36%. Furthermore, we also perturbed the volume fraction by a Gaussian random deviate with a relative standard deviation of 1.5%.

We then executed the algorithm in section 2 for each of these 100 intensity curves and calculated the range $R(q_j)$ between the minimum and maximum values of the 100 calculated intensities at q_j . In absolute terms, the range $R(q_j)$ cannot be seen on the scale of the figures presented in this paper; the largest $R(q_j)$ is more than 3000 times smaller than the peak intensity. In relative terms, the average of the ratios $R(q_j)/I(q_j)$ is 0.30%, while the median of these ratios is only 0.05%. Furthermore, the maximum ratio of 1.94% occurs at a high frequency q_j , where $I(q_j)$ is already indistinguishable from the frequency axis.

In summary, small perturbations in the input data create only small perturbations in the theoretical intensity curves. The algorithm for finding the optimal GRF model appears quite insensitive to the small errors inherent in experimental measurement.

4. Conclusions

We have used convex quadratic programming to efficiently find the optimal one-cut GRF model for fitting SANS experimental data. This algorithm permits visualizations of the aerogels which may be compared with images obtained by microscopy. This algorithm has also proven to be both versatile and robust, fitting a wide range of intensity functions and remaining mostly unchanged after small perturbations to the source intensity data.

Furthermore, visualizations produced using this algorithm may be used to initialize the stochastic optimization procedure, a more computational technique for constructing random media [31–34]. Statistical information from these GRF models, either derived theoretically from the definition of GRFs or empirically from visualizations, can be expected to predict other properties of the aerogel besides the scattering function, such as connectivity and pore-size information. Also, statistical information may be used to predict bulk properties of the aerogels, such as electrical conductivity and mechanical strength [22]. Such an analysis would provide an important check for the model's viability. These and other microstructure characterizations will be considered in future papers.

Acknowledgments

The authors are grateful to Neal Brand, W Max Jones, Jay Liu, Robert Kallman, John Neuberger and Salvatore Torquato for many helpful discussions. This material is partly based upon activities supported by the National Science Foundation under Agreement No DMR-9986442. Computational support was also provided by the Academic Computing and User Services at the University of North Texas.

References

- [1] Peltoniemi J I 1993 *J. Quant. Spectrosc. Radiat. Transfer* **50** 655
- [2] Roberts A P and Knackstedt M A 1995 *J. Mater. Sci. Lett.* **14** 1357
- [3] Roberts A P and Knackstedt M A 1996 *Physica A* **233** 848
- [4] Roberts A P and Knackstedt M A 1996 *Phys. Rev. E* **54** 2313
- [5] Knackstedt M A and Roberts A P 1996 *Macromolecules* **29** 1369
- [6] Roberts A P 1997 *Phys. Rev. E* **55** R1286
- [7] Roberts A P and Torquato S 1999 *Phys. Rev. E* **59** 4953
- [8] Roberts A P and Garboczi E J 1999 *J. Mech. Phys. Solids* **47** 2029
- [9] Biswal B, Manwart C, Hilfer R, Bakke S and Øren P E 1999 *Physica A* **273** 452
- [10] Nott D J and Rydén T 1999 *Biometrika* **86** 661
- [11] Nott D J and Wilson R J 2000 *Signal Process.* **80** 125
- [12] Bekri S, Xu K, Yousefian F, Adler P M, Thovert J F, Muller J, Iden K, Psyllos A, Stubos A K and Ionannidis M A 2000 *J. Petrol. Sci. Eng.* **25** 107
- [13] Liang Z, Ioannidis M A and Chatzis I 2000 *Chem. Eng. Sci.* **55** 5247
- [14] Roberts A P and Garboczi E J 2001 *Acta Mater.* **49** 189
- [15] Arleth A, Marčelja S and Zemb T 2001 *J. Chem. Phys.* **115** 3923
- [16] Quintanilla J, Reidy R F, Gorman B P and Mueller D W 2003 *J. Appl. Phys.* **93** 4584
- [17] Grynko Ye and Shkuratov Yu 2003 *J. Quant. Spectrosc. Radiat. Transfer* **78** 319
- [18] Shkuratov Y G and Grynko Y S 2005 *Icarus* **173** 16
- [19] Grigoriu M, Garboczi E and Kafali C 2006 *Powder Technol.* **166** 123
- [20] Quintanilla J A and Jones W M 2007 *Phys. Rev. E* at press
- [21] Guinier A, Fournet G, Walker C B and Yudowitch K L 1955 *Small-Angle Scattering of X-Rays* (New York: Wiley) chapter 2
- [22] Torquato S 2002 *Random Heterogeneous Materials: Microstructure and Macroscopic Properties* (New York: Springer) section 2.2.5
- [23] Cramér H and Leadbetter M R 1967 *Stationary and Related Stochastic Processes* (New York: Wiley) p 27
- [24] Press W H, Teukolsky S A, Vetterling W T and Flannery B P 1992 *Numerical Recipes in C: The Art of Scientific Computing* 2nd edn (New York: Cambridge University Press)
- [25] Vanderbei R J 1999 *Opt. Methods Softw.* **12** 451
- [26] Murtagh B 1981 *Advanced Linear Programming: Computation and Practice* (New York: McGraw-Hill)
- [27] Nazareth J L 1987 *Computer Solution of Linear Programs* (New York: Oxford University Press)
- [28] Reidy R, Allen A J and Krueger S 2001 *J. Non-Cryst. Solids* **285** 181
- [29] Mantoglou A and Wilson J L 1982 *Water Resour. Res.* **18** 1379
- [30] Tompson A F B, Ababou R and Gelhar L W 1989 *Water Resour. Res.* **25** 2227
- [31] Yeong C L Y and Torquato S 1998 *Phys. Rev. E* **57** 495
- [32] Cule D and Torquato S 1999 *J. Appl. Phys.* **86** 3428
- [33] Rozman M G and Utz M 2001 *Phys. Rev. E* **63** 066701
- [34] Rozman M G and Utz M 2002 *Phys. Rev. Lett.* **89** 135501